Confinement-shear lattice CSL model for fracture propagation in concrete

Gianluca Cusatis [a,*], Zdeněk P. Bažant [b], Luigi Cedolin [c]

[a] *Department of Civil and Environmental Engineering, Rensselaer Polytechnic Institute, 110 Eighth St., Troy, NY 12180, USA*
[b] *Department of Civil and Environmental Engineering, Northwestern University, 2145 Sheridan Rd., Evanston, IL 60208, USA*
[c] *Department of Structural Engineering, Politecnico di Milano University, Piazza Leonardo da Vinci 32, Milan 20133, Italy*

Abstract

A previously developed lattice model is improved and then applied to simulations of mixed-mode crack propagation in concrete. The concrete meso-structure is simulated by a three-dimensional lattice system connecting nodes which represent the centers of aggregate particles. These nodes are generated randomly according to the given grain size distribution. Only coarse aggregates are taken into account. Three-dimensional Delaunay triangulation is used to determine the lattice connections. The effective cross-section areas of connecting struts are defined by performing a three-dimensional domain tessellation partly similar to Voronoi tessellation. The deformations of each link connecting two adjacent aggregate pieces are defined in the classical manner of Zubelewicz and Bažant in which rigid body kinematics is assumed to characterize the displacement and rotation vectors at the lattice nodes. Each strut connecting adjacent particles can transmit both axial and shear forces. The adopted constitutive law simulates fracture, friction and cohesion at the meso-level. The behavior in tension and shear is made dependent on the transversal confining strain, which is computed assuming a linear displacement field within each tetrahedron of Delaunay triangulation, and neglecting the effect of the particle rotations. A mid-point explicit scheme is used to integrate the governing equations of the problems. General procedures to handle the boundary conditions and to couple the lattice mesh to the usual elastic finite element mesh are also formulated. Numerical simulations of mixed-mode fracture test data are used to demonstrate that the model is capable of accurately predicting complex crack paths and the corresponding load–deflection responses observed in experiments.
© 2005 Elsevier B.V. All rights reserved.

1. Introduction

There exist many meso-level models for simulating the behavior of concrete, and in particular fracture propagation. Each of them has its advantages and disadvantages.

One powerful approach for concrete modeling is to treat it as a material with multiphase microstructure, in which the aggregate inclusions, mortar matrix and interface layers are treated as separate phases, each of them discretized by finite elements [24,31,12]. If the inelastic and nonlinear properties of the constituents and interfaces could be realistically identified and modelled, this approach would have the potential of describing material behavior with great accuracy. Nevertheless, it would be almost prohibitive from the computational viewpoint, especially since three-dimensional discretization would be required.

---

* Corresponding author.
  E-mail addresses: cusatg@rpi.edu (G. Cusatis), z-bazant@northwestern.edu (Z.P. Bažant), cedolin@stru.polimi.it (L. Cedolin).

Lattice-particle models use, instead, a computationally more efficient approach which, despite a greatly reduced number of unknowns, can still capture the essential aspects of material heterogeneity. In this approach, the basic building blocks, the whole aggregate pieces and the layer of mortar matrix between them, represent discrete elements but are themselves not discretized on a finer scale. In these models, initiated in the mid-1980s [32], each particle connection resisted both normal and shear forces. The normal and shear displacements at the interface, placed in the middle of the connection, were figured out under the assumption of rigid particles, and the geometry of the lattice (which was only two-dimensional) was taken from photographs of actual concrete sections. Comparisons of this model to the truss models of Jirásek and Bažant [19,20] revealed that realistic modeling, especially for compression fracture, requires the lattice struts to transmit not only axial forces (as in a truss) but also shear forces (as in a frame). The shear transfer not only allows matching of the correct Poisson ratio, but it is also essential for capturing the nonlinear triaxial behavior in compression.

Subsequent lattice models of Schlangen and van Mier [27], Schlangen [25], van Mier et al. [30], and Schlangen [26] were also endowed with shear transmission capability, achieved by treating the connections as moment resisting beams in a frame. These models, which were two-dimensional, involved discretization of aggregates and mortar, and were based on mapping of the actual meso-structure. They provided very realistic cracking patterns but did not predict satisfactorily the load–displacement curves and could not handle compression failures. A recent three-dimensional version of the model [21] improves some shortcomings but still cannot simulate at the same time tensile fracture, uni- and biaxial compression failures, and over-hardening response to hydrostatic pressure and uniaxial compression strain.

The studies of Jirásek and Bažant [19,20] and Schlangen [26] also documented the importance of randomness of lattice. Although a regular lattice can be made quasi-isotropic for elastic and elasto-plastic behavior, it always engenders severe bias for the crack propagation direction.

Further important advance was achieved in the works of Bolander and Saito [9], Bolander et al. [8,10]. They formulated an irregular random lattice model with shear transfer between particles, in which the lattice geometry is obtained by means of Voronoi tessellation. Their work is remarkable for the simulation of cracking of entire structures.

The present confinement-shear lattice model (CSL model; [14,15]) is characterized by the following features:

1. It simulates the concrete meso-structure by a system of interacting aggregate particles connected by a lattice which is obtained through Delaunay triangulation of the aggregate centers.
2. The position of each aggregate piece throughout a given concrete specimen is generated randomly according to a specified granulometric distribution of aggregates.
3. The generic lattice element connecting two adjacent aggregate pieces transmits normal and shear stresses which are assumed to be functions of normal and shear strains.
4. The stresses are computed from the strains by a damage constitutive relation (similar to that used in microplane model formulation), in which the concept of stress–strain boundary (or softening yield limit) is used.
5. The constitutive behavior of each strut is softening for pure tension, tension with shear, and shear with low compression. On the contrary it is hardening for pure compression and shear with high compression.
6. The tensile and shear behaviors of the connecting struts are sensitive to the lateral confinement in directions orthogonal to the strut. This aspect is essential for capturing correct concrete behavior under unconfined compression.
7. The shear response of the connecting struts exhibits friction and cohesion.
8. The stresses act on a contact area which is defined by constructing a baricentric dual complex of the Delaunay triangulation.
9. The strains are defined by smearing over the length of each connection the relative displacements at the contact point which, in turn, are computed by assuming a rigid relative motion of the two adjacent particles.

The present model can realistically simulate [16], for concretes with fixed meso-level material parameters, all the aspects of material response, including tensile fracturing, cohesive fracture and size effect [5,23], compression-shear behavior with softening at zero or mild confinement, and highly confined or hydrostatic compression with unlimited hardening. The model has also been used to simulate the performance of headed stud anchors and has led to good agreement with the experimental evidence [13].

2. Simulation of concrete meso-structure

Six different scales of observation may be distinguished in the internal structure of concrete.

1. The atomistic scale characterized by the structure of micro-crystalline particles of hydrated Portland cement.
2. The nano-scale (whose understanding is essential for macro-scale modeling of creep, shrinkage and hygrothermal phenomena) where the main constituent is the hardened portland cement gel containing nano-pores (of up to a few nanometers in width) filled partly or fully by adsorbed water.

3. The micro-scale of several micrometers, where the main constituent is the hardened portland cement paste composed of cement gel and capillary pores containing liquid water and water vapor.
4. The mini-scale of up to several milimeters, where there is mortar, consisting of fine mineral aggregates (sand), with dimensions from 0.1 mm to about 3 mm, embedded in hardened cement paste, of which two kinds must be discerned: (a) the bulk paste, and (b) the interfacial transition zone (ITZ), with the typical width of 15–40 μm [18], which surrounds the aggregate surfaces and has a higher porosity and lower stiffness and strength than the bulk paste.
5. The meso-scale, where concrete may be regarded as a two-phase composite material consisting of coarse mineral aggregates, with sizes over 50 mm, embedded in a matrix of mortar (the coarse aggregates are also surrounded by ITZ. In this sense, the material meso-scale is better considered as a three-phase composite, although the third phase, consisting of the ITZ that is contacting only the coarse aggregates, occupies a small volume fraction).
6. The macro-scale is the usual engineering scale on which concrete is treated as a homogeneous continuum.

In this paper, we adopt and improve a recently developed random lattice model [15], which simulates concrete meso-structure and in which the customary simulation of random configuration of coarse aggregates (particles) is enhanced by introducing particle interaction laws (i.e., meso-scale constitutive laws) that take approximately into account the effect of finer-scale structure, consisting of fine aggregates (sand) in the mortar and the ITZ. These effects include the frictional shear resistance and fracturing of mortar zones connecting two large aggregate pieces, the lateral confinement of these zones by the bulk of mortar, and the effect of ITZ on connection stiffness.

The geometry of the model, for a given specimen, is defined by the following data: (1) the position of each coarse aggregate particle, (2) the connections between these particles (i.e., the topology of the interactions), and (3) the effective area through which the interaction forces between two adjacent coarse aggregate pieces are transmitted.

A typical granulometric distribution is described by the function $F(d) = (d/d_a)^n$ (Fuller curve) where d_a is the maximum aggregate size and $n \approx 0.5$. This curve can be approximated (Fig. 1) by choosing a discrete number of characteristic aggregate sizes d_i $(i = 1, \ldots, N)$ where $d_N = d_a$ and $d_1 = 4.75$ mm (i.e., the size passing sieve #4) is the threshold that conventionally separates the fine aggregates (discarded by the present model) and the coarse aggregates. The ratio of the mass of aggregates with characteristic dimension d_i to the total mass of aggregates is $\psi_i = (F_{i+1} - F_{i-1})/2$ (for $i = 2, \ldots, N-1$), $\psi_1 = (F_2 - F_1)/2$, and $\psi_N = (F_N - F_{N-1})/2$, $F_i = F(d_i)$. The number of aggregates of various sizes, which must be used to simulate a specimen of volume V, is $N_i = \psi_i a V/(\rho_a v_i)$ where v_i is the volume of one aggregate piece, ρ_a = mass density of aggregates, and a = total aggregate content, as mass per unit volume of concrete. The water–cement ratio w/c, the mass density of cement ($\rho_c \approx 3150$ kg/m^3) and the content of entrapped or entrained air can be used to get the mass density of aggregates when it is unknown [15].

To generate a statistically isotropic random microstructure, the centers of particles (aggregate pieces) of specified diameters are placed throughout the volume of the specimen one by one (from the largest to the smallest) by using a procedure introduced by Bažant et al. [6] (and also described in detail in [15]). In this procedure, after generating a new particle position by a random number generator, a check is made for possible overlaps of this particle with the previously placed particles and with the boundaries of the specimen.
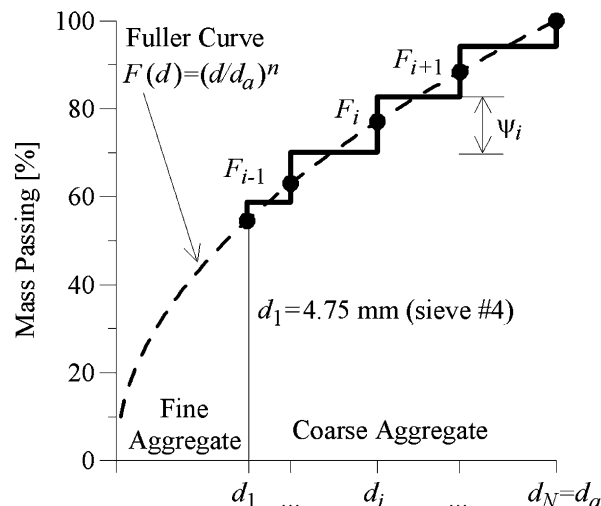

Fig. 1. Typical sieve curve (Fuller curve with $n = 0.5$) and its approximation with a discrete number of aggregate sizes.

In the original version of the present CSL model, the external surfaces of the specimen were not simulated and the boundary conditions were applied to the aggregates by a fictitious layer of material, the thickness of which was taken roughly equal to the maximum aggregate size. This approach, however, did not allow implementing general boundary conditions, and also did not give realistic results when the cross-section dimension of the simulated specimen was smaller than about five times the maximum aggregate size.

In this study, the foregoing limitations are overcome by introducing an explicit dicretization of the specimen surfaces. This is achieved by distributing over the surfaces a certain number of nodes that correspond to fictitious zero-radius particles and are automatically introduced in the numerical simulations. The accuracy of the surface representation depends on the number of these extra nodes, which increases the number of the degrees of freedom and thus affects the performance of the model. However, a surface discretization finer than the bulk discretization would, of course, be meaningless, and so it seems reasonable to consider the characteristic spacing of the surface nodes to be approximately the same as in the simulated meso-structure. Therefore, the surface nodes are placed assuming each of them to be surrounded by non-overlapping circular influence zones whose radius is equal to ξd_a ($\xi = 0.5$ works well).

The interaction among particles is based on the Delaunay triangulation [17,2], which uses as input the nodal coordinates obtained through the previously outlined procedure and gives as output three-dimensional tetrahedra which do not overlap, fill all the volume of the specimen, and have vertices coinciding with the given nodes (particle centers) and edges coinciding with the connections of adjacent nodes, called the lattice struts.

A cross-sectional area needs to be assigned to each connecting strut such that the volume of all struts be equal to the volume of the solid filled by all the tetrahedra. In Cusatis et al. [15], this goal was achieved as follows: (1) the volume of each tetrahedron was apportioned to its edges (each representing a lattice strut) proportionally to their lengths, (2) the total volume of each strut was obtained by summing up the contributions of all the adjacent tetrahedra, (3) the effective cross-sectional area of each strut was determined by dividing its volume by its length, and (4) the shape of the strut was imagined as a cylinder. The volume and the cross-section area (regarded as the area of contact between adjacent particles) assigned in this way to each strut are, of course, only approximate. In recent computations, however, it has been noticed that such an estimate of the effective cross-section area of the strut (or contact area between particles, at which a potential inter-particle crack can form) is too small, leading to unrealistic overestimation of the meso-scale stresses transmitted by the struts and across the contact area.

A more realistic estimate of the effective cross-section areas, better reflecting the random meso-structure can be obtained by using a dual complex (in the terminology of algebraic topology) of the Delaunay triangulation. A straightforward dual is the well known Voronoi tessellation. However, Voronoi tessellation is not optimal for our purpose, for at least two reasons. (1) The edge of each Voronoi cell always passes through the mid-length point of the edge of Delaunay tetrahedron, regardless of particle diameters. Thus, the effective cross-section areas, especially those for struts connecting aggregates with different diameters, are likely to intersect one of the aggregates instead of running through the mortar matrix between the particles. (2) The vertices of the Voronoi tessellation can lie outside the Delaunay tetrahedrons, in which case the edges of the tetrahedrons cannot even define the strut cross-section area (or contact area).

In the present study, a different tessellation is introduced. It is illustrated in Fig. 2 for two dimensions, and in Fig. 3 for three dimensions. Consider the two-dimensional case first. Fig. 2a shows the Delaunay triangulation of a simple two-aggregate system (P_1 and P_2) where the points P_3 and P_4 exemplify the surface nodes (particles of zero diameter). The definition of the contact line (or, in three dimensions, contact area) of the connecting strut P_1P_2 (shared by the Delaunay triangles $P_1P_2P_3$ and $P_1P_2P_4$) may be obtained by connecting the points M_{12}, G_{123} and G_{124}. Point M_{12} is located at the mid-length of the connection counterpart belonging to the matrix. Point G_{123} is the center of mass of the area obtained by subtracting
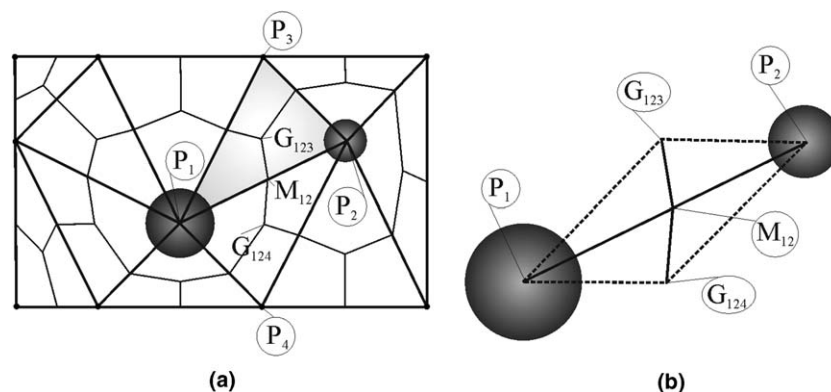

Fig. 2. (a) Example of two-dimensional tessellation of concrete meso-structure. (b) Geometry of a connecting strut.
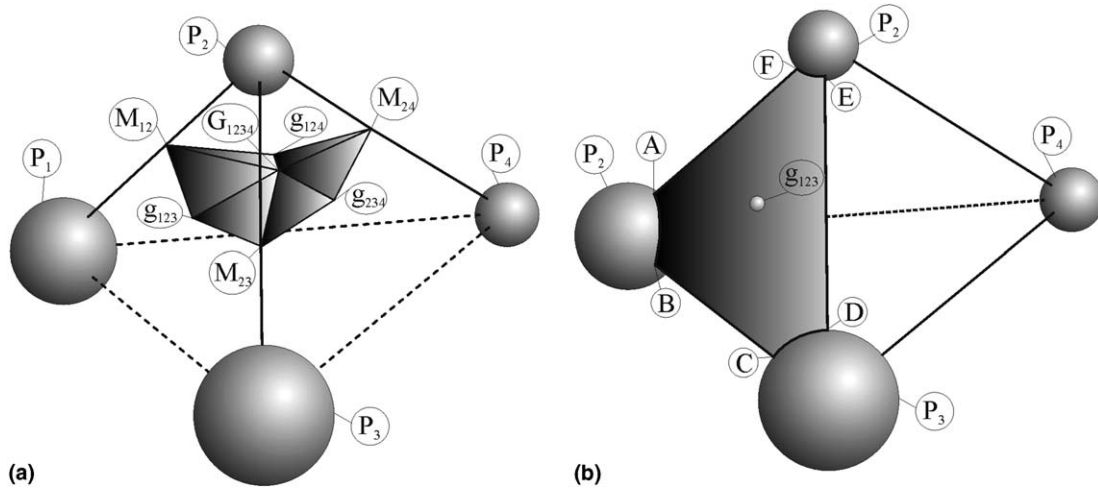
Fig. 3. Definition of the characteristic points of the three-dimensional tessellation.

from the area of triangle $P_1P_2P_3$ the counterparts of the aggregate areas (circular sectors) associated with that triangle; point G_{124} is similar to point G_{123} but related to triangle $P_1P_2P_4$. By connecting points G_{123} and G_{124} to the aggregate centers (Fig. 2b), it is also possible to define realistically the area (or volume, in three dimensions) associated with the connection P_1P_2. This procedure can be applied to any of the connections emanating from a particle (either actual aggregate pieces or surface nodes). In this way, one obtains a complete tessellation of the domain, in which each particle is contained within one and only one cell.

Extension to the three-dimensional case is quite straightforward. Fig. 3a shows a tetrahedron connecting four particles $(P_1, \ldots, P_4)$ along with the counterpart of the contact areas (or potential crack areas) associated with this tetrahedron and belonging to the connections P_1P_2, P_2P_3 and P_2P_4 (similar contact areas can be defined for the connections P_1P_3, P_1P_4 and P_3P_4, but, for sake of clarity, they are not shown). Points M_{ij} $(i,j = 1, \ldots, 4)$ have the same meaning as in two dimensions. Point G_{1234} is now the center of mass of the volume obtained by subtracting from the volume of the tetrahedron the counterparts of the aggregate volumes (spherical sectors) associated with that tetrahedron. Points g_{ijk} $(i,j,k = 1, \ldots, 4)$ are peculiar to the three-dimensional tessellation and are defined on each triangular face of the tetrahedron in the same way as point G_{123} was defined in two dimensions. They are, in fact, the centers of mass of the areas obtained by subtracting from the areas of the triangular faces the areas of the circular sectors defined by the intersection with the aggregate spheres (e.g., area ABCDEF in Fig. 3b for the $P_1P_2P_3$ face). Fig. 4 shows a three-dimensional cell, containing an aggregate piece with several emanating connections, obtained by the previous tessellation procedure. Each cell (an aggregate inclusion with its surrounding matrix) has its own random irregular shape. This property is very important to ensure a realistic representation of the kinematics of concrete meso-structure, and especially to avoid excessive rotations of particles, which plagued the numerical simulations when regularly shaped particle systems were used [28].
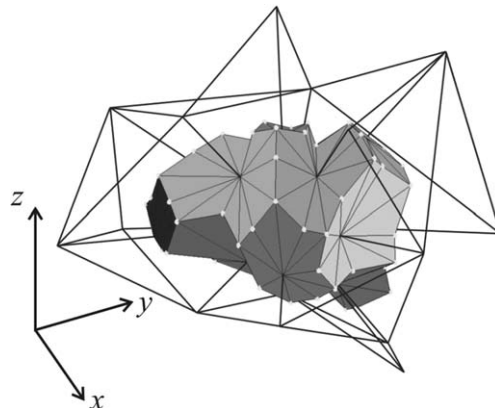

Fig. 4. Three-dimensional cell containing an aggregate.

3. Kinematics and statics of the model

The contact areas of the connecting struts emanating from each aggregate are, in general, not planar and not orthogonal to the connection (Fig. 5a). For the sake of simplicity, the constitutive law is imposed on a projection of this area on a plane orthogonal to the connection and containing point M of the tessellation (Fig. 5b). The contact point C considered as the center of mass of the projected area, is no longer located along the connection axis (P_1P_2), as it was in the previous version of the model. Along the connection, aggregates and matrix are considered to be coupled in series (and the effect of the ITZ is also embedded in this coupling). The overall response of the connection is lumped into a zero-thickness link element located at the contact point. This has the advantage that the displacements in the connection can then be expressed from relative rigid body movements of the two parts of the strut;

$$\mathbf{u}(\mathbf{x}) = \mathbf{u}_I + \boldsymbol{\theta}_I \times (\mathbf{x} - \mathbf{x}_I) = \mathbf{A}_I(\mathbf{x})\mathbf{Q}_I, \tag{1}$$

where

$$\mathbf{A}_I(\mathbf{x}) = \begin{bmatrix} 1 & 0 & 0 & 0 & z - z_I & y_I - y \\ 0 & 1 & 0 & z_I - z & 0 & x - x_I \\ 0 & 0 & 1 & y - y_I & x_I - x & 0 \end{bmatrix}. \tag{2}$$

The vectors $\mathbf{x} = [x \ y \ z]^T$, $\mathbf{u} = [u_x \ u_y \ u_z]^T$ and $\boldsymbol{\theta} = [\theta_x \ \theta_y \ \theta_z]^T$ collect the spatial coordinates, the displacements and the rotations, respectively, of a generic point belonging to the strut. Subscript I can be equal to 1 or 2 depending on whether $\mathbf{x}$ represents the position of a point located between the contact point C and the aggregate P_1 or P_2, respectively. In Eq. (1), the symbol $\times$ represents the vectorial cross product and the vector $\mathbf{Q}_I = [\mathbf{u}_I^T \ \boldsymbol{\theta}_I^T]^T$ collects all the degrees of freedom of node (particle) I (Fig. 5c).
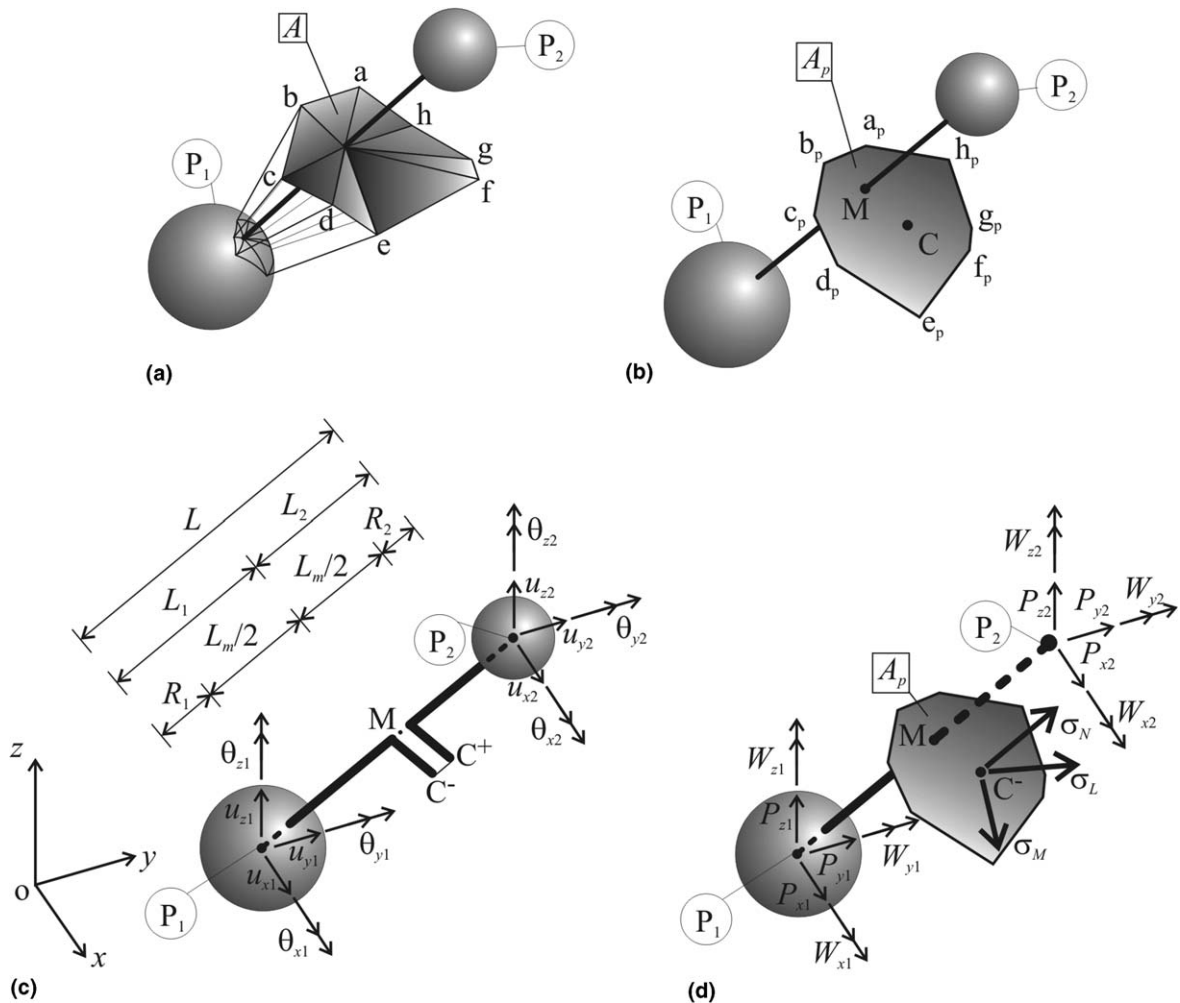

Fig. 5. (a) Contact area (potential crack surface) between two adjacent aggregates; (b) projected contact area; (c) geometry and degrees of freedom of a connecting strut; (d) stresses acting on the contact area and related nodal forces.

The displacement jump at the contact point can be computed as

$$[\![\mathbf{u}_C]\!] = \mathbf{u}(\mathbf{x}_C^+) - \mathbf{u}(\mathbf{x}_C^-) = \mathbf{A}_2(\mathbf{x}_C)\mathbf{Q}_2 - \mathbf{A}_1(\mathbf{x}_C)\mathbf{Q}_1. \tag{3}$$

By using Eq. (3) we can define the normal strain and the shear strains as follows:

$$\varepsilon_N = \mathbf{n}^{\mathrm{T}}[\![\mathbf{u}_C]\!]/\ell = \mathbf{B}_{N2}\mathbf{Q}_2 - \mathbf{B}_{N1}\mathbf{Q}_1, \tag{4}$$

$$\varepsilon_L = \mathbf{l}^{\mathrm{T}}[\![\mathbf{u}_C]\!]/\ell = \mathbf{B}_{L2}\mathbf{Q}_2 - \mathbf{B}_{L1}\mathbf{Q}_1, \tag{5}$$

$$\varepsilon_M = \mathbf{m}^{\mathrm{T}}[\![\mathbf{u}_C]\!]/\ell = \mathbf{B}_{M2}\mathbf{Q}_2 - \mathbf{B}_{M1}\mathbf{Q}_1. \tag{6}$$

We have set $\mathbf{B}_{NI} = (1/\ell)\mathbf{n}^{\mathrm{T}}\mathbf{A}_I(\mathbf{x}_C)$, $\mathbf{B}_{LI} = (1/\ell)\mathbf{l}^{\mathrm{T}}\mathbf{A}_I(\mathbf{x}_C)$, and $\mathbf{B}_{MI} = (1/\ell)\mathbf{m}^{\mathrm{T}}\mathbf{A}_I(\mathbf{x}_C)$ where ℓ is the length of the connecting strut. The unit vector $\mathbf{n}$ is orthogonal to the contact area and is defined as $\mathbf{n} = (\mathbf{x}_2 - \mathbf{x}_1)^{\mathrm{T}}(\mathbf{x}_2 - \mathbf{x}_1)/\ell$. The unit vectors $\mathbf{l}$ and $\mathbf{m}$ are mutually orthogonal and both tangential to the contact area.

In similarity to the previous formulation of the model, the following three measures of strain have been defined: $\varepsilon_{\mathrm{T}} = \sqrt{\varepsilon_M^2 + \varepsilon_L^2}$, $\varepsilon = \sqrt{\varepsilon_N^2 + \alpha\varepsilon_{\mathrm{T}}^2}$ and $\tan\omega = \varepsilon_N/(\sqrt{\alpha}\varepsilon_{\mathrm{T}})$ where ε_{T} is the total shear strain. The strain ε is the so-called effective strain [11,15], ω is the so-called coupling strain [15], and α is a material parameter.

The stresses σ_N, σ_L and σ_M are conjugate to the strains ε_N, ε_L and ε_M, respectively, and are depicted in Fig. 5d. The total shear stress σ_{T} that is conjugate to ε_{T} according to the principle of virtual power applied to the shear components reads: $\sigma_{\mathrm{T}} = \sqrt{\sigma_M^2 + \sigma_L^2}$. Stress σ (called the effective stress) is conjugate to ε, and stress τ is conjugate to ω; they must satisfy the principle of virtual power applied to the normal and the shear components. After some algebraic calculations, and upon assuming that $\tau(\varepsilon,\omega) \equiv 0$ [15], one gets $\sigma_N = \sigma\varepsilon_N/\varepsilon$, $\sigma_M = \sigma\alpha\varepsilon_M/\varepsilon$, and $\sigma_L = \sigma\alpha\varepsilon_L/\varepsilon$. Note that, by virtue of the previous expression, the coupling strain can also be expressed in terms of the stresses as $\tan\omega = \sqrt{\alpha}\sigma_N/\sigma_{\mathrm{T}}$.

The nodal forces can be computed by the principle of virtual power, which gives

$$\mathbf{F}_1^{\mathrm{T}}\dot{\mathbf{Q}}_1 + \mathbf{F}_2^{\mathrm{T}}\dot{\mathbf{Q}}_2 = A_{\mathrm{p}}\ell(\sigma_N\dot{\varepsilon}_N + \sigma_L\dot{\varepsilon}_L + \sigma_M\dot{\varepsilon}_M), \tag{7}$$

where A_{p} is the projected contact area, and the vector $\mathbf{F}_I^{\mathrm{T}} = [\mathbf{P}_I^{\mathrm{T}} \ \mathbf{W}_I^{\mathrm{T}}]$ collects the forces, $\mathbf{P}_I^{\mathrm{T}} = [P_{xI} \ P_{yI} \ P_{zI}]$ and $\mathbf{W}_I^{\mathrm{T}} = [W_{xI} \ W_{yI} \ W_{zI}]$, conjugate to the nodal degrees of freedom (Fig. 5d). After substituting Eqs. (4)–(6) into Eq. (7), we eventually get

$$\mathbf{F}_1 = -A_{\mathrm{p}}\ell(\sigma_N\mathbf{B}_{N1} + \sigma_M\mathbf{B}_{M1} + \sigma_L\mathbf{B}_{L1})^{\mathrm{T}}, \tag{8}$$

$$\mathbf{F}_2 = A_{\mathrm{p}}\ell(\sigma_N\mathbf{B}_{N2} + \sigma_M\mathbf{B}_{M2} + \sigma_L\mathbf{B}_{L2})^{\mathrm{T}}. \tag{9}$$

4. Constitutive law with confinement effect

The constitutive law is defined on the meso-level and is, for the most part, taken from Cusatis et al. [15], which gives the details. Here we highlight its main features, and also present some improvements.

The elastic behavior can be characterized as $\sigma = E\varepsilon$ or equivalently as $\sigma_N = E\varepsilon_N$, $\sigma_L = E_{\mathrm{T}}\varepsilon_L$ and $\sigma_M = E_{\mathrm{T}}\varepsilon_M$ where $E_N = E$, $E_{\mathrm{T}} = \alpha E$. Throughout the connecting strut, the aggregates and the matrix, represented by segments $\ell_a = R_1 + R_2$ and ℓ_{m}, respectively (Fig. 5c), are assumed to act in series. Approximately, we can write $E = \ell/(\ell_a/E_a + \ell_{\mathrm{m}}/E_{\mathrm{m}})$ where the elastic parameters E_a and E_{m} characterize the elastic properties of aggregates and matrix. The constant α should, in principle, be also considered to depend on the elastic properties of concrete constituents but is assumed as constant since it governs the macroscopic Poisson ratio which is nearly the same for all normal concretes—about 0.18, which is obtained for $\alpha = 0.25$.

The inelastic behavior, simulating damage, fracture and plasticity at the meso-level, is formulated assuming the effective stress σ to be governed by a strain-dependent boundary, which is expressed, for non-cyclic loadings, as

$$\sigma_{\mathrm{b}}(\varepsilon,\omega) = \sigma_0(\omega)\exp\left\{\frac{K(\omega)}{\sigma_0(\omega)}\left\langle\varepsilon - \frac{\sigma_0(\omega)}{E}\right\rangle\right\} \tag{10}$$

in which $\langle\bullet\rangle = \max\{\bullet, 0\}$. Function $\sigma_0(\omega)$ is the initial effective strength function, which delimits the elastic domain in the stress space (Fig. 6a). It is assumed to be a hyperbola with an ellipsoidal cap in compression. Its expression depends on the following meso-level material properties: tensile strength σ_{t}, shear strength σ_{s}, compressive strength σ_{c}, slope μ of the hyperbola asymptote and aspect ratio β of the ellipsoidal cap.

For $\omega \leqslant \omega_0$ there is hardening, and for $\omega > \omega_0$ softening, where ω_0 (<0) gives the intersection between the two functions (hyperbola and ellipse) defining the strength function $\sigma_0(\omega)$. The initial hardening-softening modulus is given by the function $K(\omega)$ (initial slope function) which is defined as (Fig. 6b):
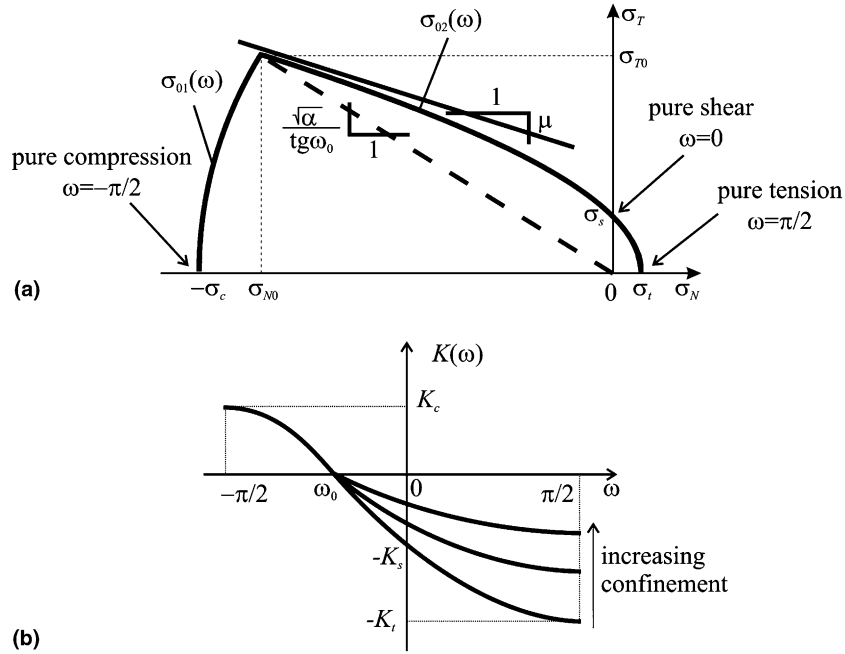
Fig. 6. (a) Elastic domain at the meso-level. (b) Initial slope function.

$$
K(\omega) = \begin{cases} K_c \left[1 - \left(\dfrac{\omega + \pi/2}{\omega_0 + \pi/2} \right)^{n_c} \right] & \text{for } \omega \leqslant \omega_0, \\[4mm] -K_t f(\lambda) \left[1 - \left(\dfrac{\omega - \pi/2}{\omega_0 - \pi/2} \right)^{n_t} \right] & \text{for } \omega > \omega_0. \end{cases} \tag{11}
$$

Parameters K_c and n_c govern the nonlinear compressive and shear-compressive behavior ($\omega \leqslant \omega_0$) at meso-level. On the contrary, parameters K_t and n_t mainly govern the nonlinear tensile and shear-tensile behavior at meso-level.

For $\omega > \omega_0$, which includes pure shear ($\omega = 0$) and pure tension ($\omega = \pi/2$), the post-peak slope is made sensitive to the confinement transversal to the connection. This dependence is justified by the fact that the degree of transversal confinement must affect the resistance to frictional pullout of crack-bridging fragments and small aggregate pieces, which is known to cause that the softening is gradual rather than sudden. The confinement effect is introduced in the formulation in Eq. (11) through the function

$$
f(\lambda) = \frac{1}{1 + \langle -\lambda/\lambda_0 \rangle}, \tag{12}
$$

where λ is the confinement strain in each strut obtained by projecting orthogonally to the connection the average of the strain tensors of the adjacent tetrahedra. In turn, the strain tensor in each tetrahedron is computed assuming a linear distribution of displacements and neglecting the effect of particle rotations. The characteristic strain parameter λ_0 governs the sensitivity to confining strain. The use of the confining strain instead of the confining stress [15] is, from a computational viewpoint, very effective. It allows explicit calculation of stresses from strains (i.e., a fully explicit formulation), and makes the numerical algorithm more robust.

In absence of confinement ($\lambda = 0$ and $f(\lambda) = 1$), we assume the meso-level fracturing behavior to be governed by the meso-level fracture energies G_t for mode I and G_s for mode II (regarded here as basic material properties). Thus, in order to preserve the correct energy dissipation, the integral of the stress–strain curve for $\omega = 0$ (pure shear) and for $\omega = \pi/2$ (pure tension) must be equal to G_s and G_t, respectively, divided by the length of the connection [3]. Since the stress–strain relation is exponential, we get

$$
-K(0) = K_s = \frac{2\alpha E}{\ell_s^{cr}/\ell - 1}; \quad -K(\pi/2) = K_t = \frac{2E}{\ell_t^{cr}/\ell - 1}; \quad n_t = \frac{\ln[K_t/(K_t - K_s)]}{\ln(1 - 2\omega_0/\pi)}, \tag{13}
$$

where $\ell_s^{cr} = 2\alpha E G_s/\sigma_s^2$ and $\ell_t^{cr} = 2E G_t/\sigma_t^2$ are two characteristic lengths of the material.

5. Boundary conditions and coupling with usual finite elements

In this section, two algorithms are proposed for applying boundary conditions to random lattice meshes in the framework of the central difference scheme, used here to integrate the differential equations of dynamic equilibrium. The first algorithm is intended for boundary conditions simulating very stiff loading platens that can be approximated as rigid. The second algorithm is more general and is based on coupling the lattice mesh with the usual finite element mesh.

The equations of the central difference method can be summarized as follows [29]:

$$\dot{Q}_I^{n+1/2} = a\dot{Q}_I^{n-1/2} + b\frac{P_I^n - F_I^n}{M_I} \tag{14}$$

for unconstrained degrees of freedom and

$$\dot{Q}_I^{n+1/2} = \dot{\delta}_I^{n+1/2},$$
$$R_I^n = P_I^n + M_I(\dot{\delta}_I^{n+1/2} - a\dot{\delta}_I^{n-1/2})/b \tag{15}$$

for constrained degrees of freedom; subscript I identifies the generic degree of freedom; superscript n labels the nth time step Δt used to discretize the time history; $a = 0$, $b = \Delta t/2$ for $n = 0$ and $a = (1 - v)/(1 + v)$, $b = \Delta t/(1 + v)$ for $n \neq 0$, $v = C\Delta t/2$ and $C =$ damping coefficient (in all numerical calculations it is assumed that $C = 0$). Symbols P_I, F_I, M_I represent the internal force, the external force and the mass of the Ith degree of freedom. In Eq. (15), the velocity $\dot{\delta}_I$ is known (from the kinematic boundary condition) and R_I is the reaction force arising at the boundary.

Consider now the case of a rigid loading platen loaded under displacement control. If the platen is not rotating, each lattice node underneath the platen has the same displacement and then Eq. (15) can be directly applied. However, in material testing, the load is often applied to the loading platen through a hinge, so that the platen could freely rotate. In that case, the lattice nodes directly in contact with the platens experience different displacements that are functions of the unknown rotations of the platen. For these nodes, one may write (Fig. 7a):

$$\dot{\delta}_J(t) = \dot{\delta}(t) + \dot{\theta}_x(t)y_J - \dot{\theta}_y(t)x_I, \tag{16}$$

where δ, θ_x and θ_y are the known displacement and the unknown rotations, respectively, of the loading platen. Subscript J identifies the degree of freedom in the direction of the applied boundary condition. The unknown platen rotations at time $t_{n+1/2}$ can be computed upon setting the reaction moments at time t_n to zero. By introducing Eqs. (15) and (16) into the equations $\sum_J R_J^n y_J = 0$ and $\sum_J R_J^n x_J = 0$, we get

$$\dot{\theta}_x^{n+1/2} = \frac{A_{22}B_1 - A_{12}B_2}{A_{11}A_{22} - A_{12}A_{21}}; \quad \dot{\theta}_y^{n+1/2} = \frac{-A_{21}B_1 + A_{11}B_2}{A_{11}A_{22} - A_{12}A_{21}}, \tag{17}$$

where $A_{11} = \sum_J M_J y_J^2/b$, $A_{12} = A_{21} = \sum_J M_J x_J y_J/b$, $A_{22} = \sum_J M_J x_J^2/b$, $B_1 = -\sum_J[P_J^n y_J + M_I y_J(-a\dot{\delta}_J^{n-1/2} + \dot{\delta}^{n+1/2})/b]$, and $B_2 = \sum_J P_J^n x_J + M_J x_J(-a\dot{\delta}_J^{n-1/2} + \dot{\delta}^{n+1/2})/b$.

Small modifications to the previous equations further allow simulating the case of a rigid platen under load control, and switching from displacement control to load control and vice versa during the simulation.

It can also happen that the loading device is not stiff enough to be considered as rigid. In that case, it is necessary to simulate the loading platens by usual finite elements and to couple them with the lattice mesh. Coupling the usual finite element meshes and lattice meshes can also be used to reduce the computational cost when the damage localizes in a small zone the location of which is known in advance (as in notched specimens). In that situation, it is reasonable to use the lattice model only where nonlinear material behavior is expected, and to discretize the rest of the structure by elastic finite elements.
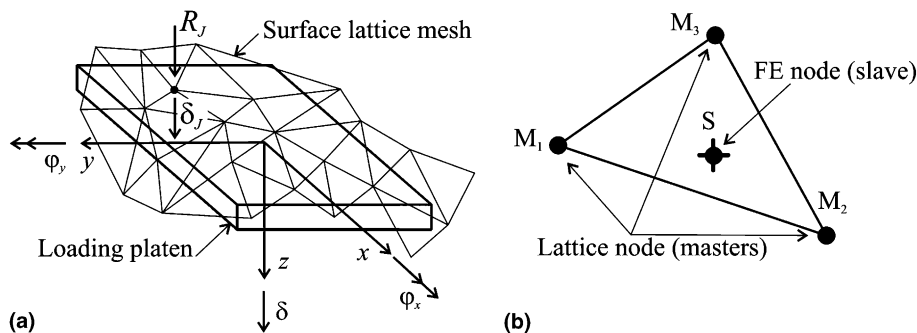

Fig. 7. (a) Degrees of freedom of a rigid loading platen. (b) Master–slave connection.

At the interface, the nodes of a finite element mesh and a lattice mesh generally do not coincide since the nodes simulating concrete are randomly located on the surface. To handle this problem, we use the so-called 'master–slave' approach [7]. Each interface node belonging to the finite element mesh (slave node) is considered constrained to the three concrete nodes (master nodes) defining the triangle on which the finite element node is included (Fig. 7b). One can write

$$\mathbf{u}_S = \mathbf{\Phi}\mathbf{u}_M \tag{18}$$

in which vector $\mathbf{u}_S$ collects the displacements of the slave node and $\mathbf{u}_M$ collects the displacements of the three master nodes; $\mathbf{\Phi} = [\mathbf{\Phi}_1 \ \mathbf{\Phi}_2 \ \mathbf{\Phi}_3]$, $\mathbf{\Phi}_i = \mathrm{diag}[\varphi_1; \varphi_2; \varphi_3]$; and φ_i is the linear shape function associated with master node i $(i = 1, \ldots, 3)$.

The internal forces $\mathbf{P}_M$ at the master nodes, which include the effect of the slave nodes, can be calculated from the principle of virtual work by imposing the condition that

$$\mathbf{u}_M^T \mathbf{P}_M = \mathbf{u}_M^T \hat{\mathbf{P}}_M + \mathbf{u}_S^T \hat{\mathbf{P}}_S, \tag{19}$$

where $\hat{\mathbf{P}}_M$ and $\hat{\mathbf{P}}_S$ are the internal forces of the master and slave nodes, respectively, considered unconstrained.

By substituting Eq. (18) into Eq. (19), one gets

$$\mathbf{P}_M = \hat{\mathbf{P}}_M + \mathbf{\Phi}^T \hat{\mathbf{P}}_S. \tag{20}$$

The internal forces can then be assembled in the global internal force vector.

If the finite element mesh behaves elastically, then the internal forces $\hat{\mathbf{P}}_S$ can be efficiently computed at each loading step by using the well-known static condensation procedure. The stiffness matrix of the finite element mesh $\mathbf{K}$ can be partitioned as follows:

$$\mathbf{K} = \begin{bmatrix} \mathbf{K}_{11} & \mathbf{K}_{12} & \mathbf{K}_{13} \\ \mathbf{K}_{21} & \mathbf{K}_{22} & \mathbf{K}_{23} \\ \mathbf{K}_{31} & \mathbf{K}_{32} & \mathbf{K}_{33} \end{bmatrix}, \tag{21}$$

where the first row is associated with the degrees of freedom of the nodes at which the kinematic boundary conditions are applied, which are collected in vector $\mathbf{U}_1$ (if static boundary conditions are applied, a small modification of the algorithm can handle them, too). The third row is associated with the degrees of freedom (collected in the vector $\mathbf{U}_3$) of the nodes at the bottom of the mesh, connected to the concrete (lattice) mesh. The second row is associated with all remaining degrees of freedom collected in the vector $\mathbf{U}_2$. Since no external loads are associated with the degrees of freedom in $\mathbf{U}_2$, we can write

$$\mathbf{P}_1 = \mathbf{K}_{11}\mathbf{U}_1 + \mathbf{K}_{12}\mathbf{U}_2 + \mathbf{K}_{13}\mathbf{U}_3, \tag{22}$$

$$\mathbf{K}_{21}\mathbf{U}_1 + \mathbf{K}_{22}\mathbf{U}_2 + \mathbf{K}_{23}\mathbf{U}_3 = \mathbf{0}, \tag{23}$$

$$\mathbf{P}_3 = \mathbf{K}_{31}\mathbf{U}_1 + \mathbf{K}_{32}\mathbf{U}_2 + \mathbf{K}_{33}\mathbf{U}_3, \tag{24}$$

where $\mathbf{P}_1$ are the reaction forces at the boundary and $\mathbf{P}_3$ collects the vectors $\hat{\mathbf{P}}_S$ of all the slave nodes (i.e., the finite element nodes located at the interface between the lattice mesh and the finite element mesh).

By solving $\mathbf{U}_2$ from Eq. (23) we get

$$\mathbf{U}_2 = \mathbf{A}_{21}\mathbf{U}_1 + \mathbf{K}_{23}\mathbf{U}_3, \tag{25}$$

where $\mathbf{A}_{21} = -\mathbf{K}_{22}^{-1}\mathbf{K}_{21}$ and $\mathbf{A}_{23} = -\mathbf{K}_{22}^{-1}\mathbf{K}_{23}$. By substituting Eq. (25) into Eqs. (22) and (24), we eventually obtain

$$\mathbf{P}_1 = \mathbf{A}_{11}\mathbf{U}_1 + \mathbf{A}_{13}\mathbf{U}_3, \tag{26}$$

$$\mathbf{P}_3 = \mathbf{A}_{31}\mathbf{U}_1 + \mathbf{A}_{33}\mathbf{U}_3, \tag{27}$$

where $\mathbf{A}_{11} = \mathbf{K}_{11} + \mathbf{K}_{12}\mathbf{A}_{21}$, $\mathbf{A}_{13} = \mathbf{K}_{13} + \mathbf{K}_{12}\mathbf{A}_{23}$, $\mathbf{A}_{31} = \mathbf{K}_{31} + \mathbf{K}_{32}\mathbf{A}_{21}$, $\mathbf{A}_{33} = \mathbf{K}_{33} + \mathbf{K}_{32}\mathbf{A}_{23}$.

6. Four-point-shear test

Let us now analyze the four-point-shear test that has often been used to study mixed mode fracture propagation in concrete. In particular we try to simulate the experimental data by Ballatore et al. [1]. Fig. 8a shows the adopted setup in which a double-notched prismatic specimen was tested by applying the load, by means of a steel beam, to two points (1 and 2 in Fig. 8a) at the top side of the specimen. The test was conducted by controlling the displacement of the actuator (displacement δ in Fig. 8a). The ratio between the forces acting at the two points was $F_1/F_2 = c/S$, where c indicates the distance between the bottom support and the top loading point close to the notches, and S is the span. The span-to-depth ratio (S/D) was always kept equal to 4 during the experiments while different values of the ratio c/D were investigated. In the following, we will consider the ratios $c/D = 0.2$ and $c/D = 0.4$, which lead to $F_2 = 0.05\,F_1$ and $F_2 = 0.1F_1$, respectively. The thickness of all the specimens tested was 100 mm and the notch depth was $0.2D$.
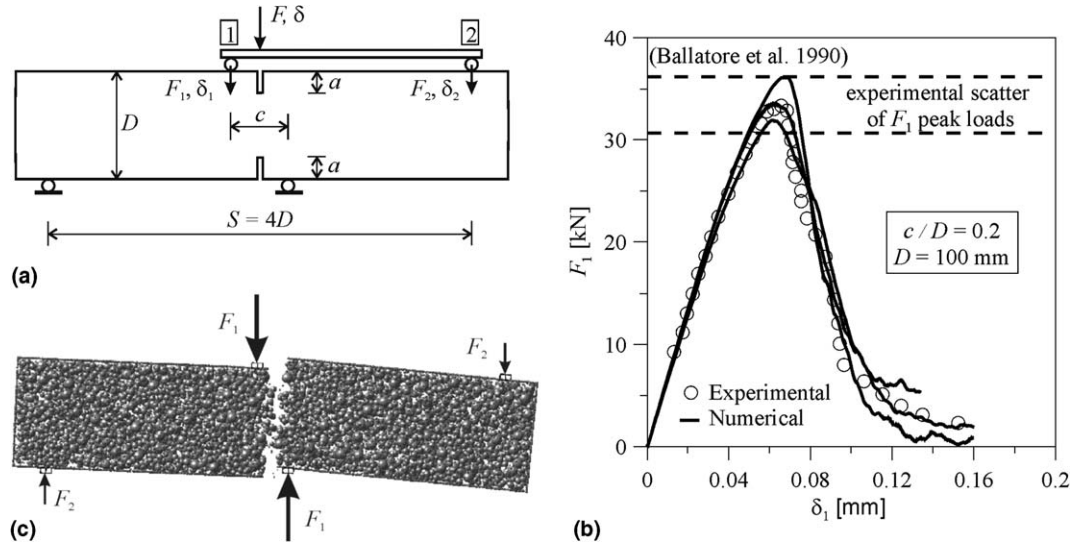
Fig. 8. Four-point shear test: (a) test setup, (b) load–displacement curve for $c/D = 0.2$, $D = 100$ mm, and (c) displaced configuration at failure for $c/D = 0.2$, $D = 100$ mm.

Table 1
Experimental and numerical mechanical properties of simulated concrete

	E [GPa]	f_c [MPa]	f_t [MPa]	G_F^{tens} [N/m]
Ballatore et al. [1]	36.53	51.73	2.18	93.0
Lattice simulation	35.81	48.23	2.10	91.5

The mix-design of the concrete used to cast the specimens was as follows: cement content = 460 kg/m³, water–cement ratio = 0.46, aggregate–cement ratio = 3.65, and maximum aggregate size $d_a = 10$ mm. The related mechanical properties are summarized in the first row of Table 1 in which E is the elastic modulus, f_c is the compressive strength (measured on 100 mm-side cubes), f_t is the tensile strength (measured on prisms with square cross-section of a side of 100 mm), and G_F^{tens} is the fracture energy measured by direct tension on notched cylindrical specimen with a diameter of 100 mm and length of 200 mm.

The lattice simulation is carried out considering the mass fraction of aggregates with the characteristic sizes of 10 mm, 6.35 mm and 4.75 mm to be 16%, 10% and 5%, respectively. The model parameters, optimized by fitting the measured mechanical properties (Table 1, second row) are as follows: elastic parameters $E_c = 37$ GPa and $E_a = 3E_c$, coupling parameter $\alpha = 0.25$, tensile meso-strength (strength at meso-level of microstructure) $\sigma_t = 2.2$ MPa, meso-cohesion $\sigma_s = 3\sigma_t$, mode-I fracture energy at meso-level $G_t = 0.03$ N/mm, mode-II fracture energy at meso-level $G_s = 16G_t$, characteristic strain for confinement effect $\lambda_0 = 1 \times 10^{-3}$, compressive meso-strength $\sigma_c = 40\sigma_t$, hardening parameter at meso-level $K_c = 0.26E_c$, shape parameter of compression cap $\beta = 1$, slope of the hyperbola asymptote $\mu = 0.2$, and $n_c = 2$. In numerical simulations, the bottom supports are assumed to be sliding.

Fig. 8b shows the load–displacement curves (in terms of force, F_1, and displacement, δ_1, at point 1) of the specimen with $D = 100$ mm and $c/D = 0.2$. The numerical results (shown by black lines corresponding to three different randomly generated meso-structures) are compared with the experimental data, and the agreement is good. The (enlarged) displaced configuration at failure is shown in Fig. 8c. The failure mode, characterized by a crack connecting the two notches, agrees with the experimental evidence and was also observed by Bažant and Pfeiffer [4]. Fig. 9a and b show the distribution of damage at peak load and a the post-peak state. Damage is represented by spheres of different color graded by a gray scale: black spheres represent fully damaged material and white spheres represent undamaged material. At the peak, one can see two inclined cracks developing from the notch tips and triggered by the stress concentration, and a zone of diffuse damage spreading along the ligament. In the post-peak, on the contrary, only a damage band connecting the two notches can be clearly seen.

To explore the nature of these damage patterns, we can look at the evolution of the dissipated energy by the normal components ($W_{d,N}$) and the tangential components ($W_{d,T}$) of the lattice elements (Fig. 9c). We may note that although, in general, $W_{d,N}$ sums up the energies dissipated in both tension and compression, in the present simulations it almost coincides with the energy dissipated in tension because the energy dissipated in compression is negligible. Up to the peak, the energy dissipated in tension and that dissipated in shear have nearly the same value, which proves that failure implies both
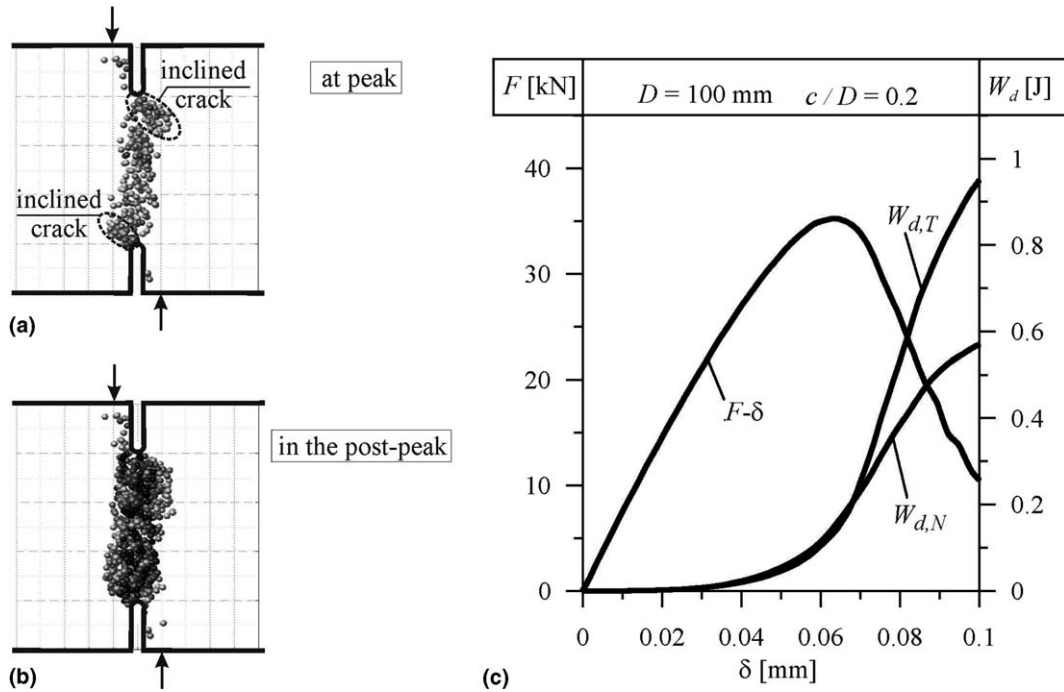
Fig. 9. Four-point shear test with $c/D = 0.2$, $D = 100$ mm: (a) damage distribution at peak, (b) damage distribution in the post-peak, and (c) evolution of the dissipated energy.

mode I and mode II crack propagation in the meso-structure. Furthermore, the effect of mode II crack propagation at the mesolevel is even more pronounced in the post-peak when the energy dissipated in shear becomes significantly larger than that dissipated in tension. We must also observe that, in the softening regime, the evolution of the system is dynamic rather than static. This is due to the type of test control (the displacement of the actuator) used in the experiments which is known to be unstable for this kind of tests (see e.g. [25,27]). Static equilibrium paths can be followed if the test is controlled by the relative displacements of the crack mouth as done in Schlangen [25] and Schlangen and van Mier [27] who reported the initiation of two cracks at the notch tips and the subsequent evolution of just one crack.

Fig. 10 presents the numerical results obtained for beams with $c/D = 0.4$ and three different depths, namely $D = 50$ mm (small), 100 mm (medium) and 200 mm (large). Fig. 10a compares the numerical load–displacement curves (in terms of the total applied force, $F = F_1 + F_2$, and of displacement, δ, at the point of application of F) of the three specimens of different sizes with the measured peak loads. Once more, the agreement is satisfactory.

It is interesting to analyze the effect of specimen size on the failure mode, reported by Ballatore et al. [1]. In the medium-size specimens ($D = 100$ mm), two cracks propagated from the opposite notch tips along curved paths towards the opposite side of the specimen and bypassed each other. By contrast, in the large-size specimens ($D = 200$ mm), only one crack reached the opposite surface of the specimen, leading to failure. The CSL model reproduces this behavior exactly, as one can see in Fig. 10c and d. The numerical simulations show that, for the medium-size specimen, the fracture process is almost quasi-static, with little kinetic energy generated in the post-peak. For the large-size specimen, instead, the fracture development is truly dynamic and a significant amount of kinetic energy is released in the softening regime.

The different modes of failure of medium-size and large-size specimens are further analyzed in Figs. 11 and 12. Fig. 11a and b present the load–displacement curves at the loading points 1 and 2 ($F_1 - \delta_1$ and $F_2 - \delta_2$), obtained in one of the three simulations for the medium- and large-size specimens, respectively. For the medium-size specimen, displacements δ_1 and δ_2 are always increasing. However, for the large-size specimen, only displacement δ_2 is always increasing while displacement δ_1 at a certain point begins to decrease, unloading towards the origin. Note also that, in both cases, the displacement of the actuator, δ, is always increasing, being the variable directly controlled during the test.

The difference in the behavior of the medium- and large-size specimens can be also meaningfully analyzed looking at the evolution of the internal energy W_{int} and the dissipated energy W_{d}. In Fig. 11c and d, the continuum lines represent the total internal energy and the internal energy associated with the normal and tangential components in the lattice elements. The dashed lines are the corresponding dissipated energies. Obviously, for both medium and large size specimens, the dissipated energies are always increasing. The internal energies are always increasing for the medium-size specimens. On the contrary, for the large-size specimen the internal energy associated with the normal component in the lattice elements and the total internal energy have a local maximum corresponding to unloading at point 1.
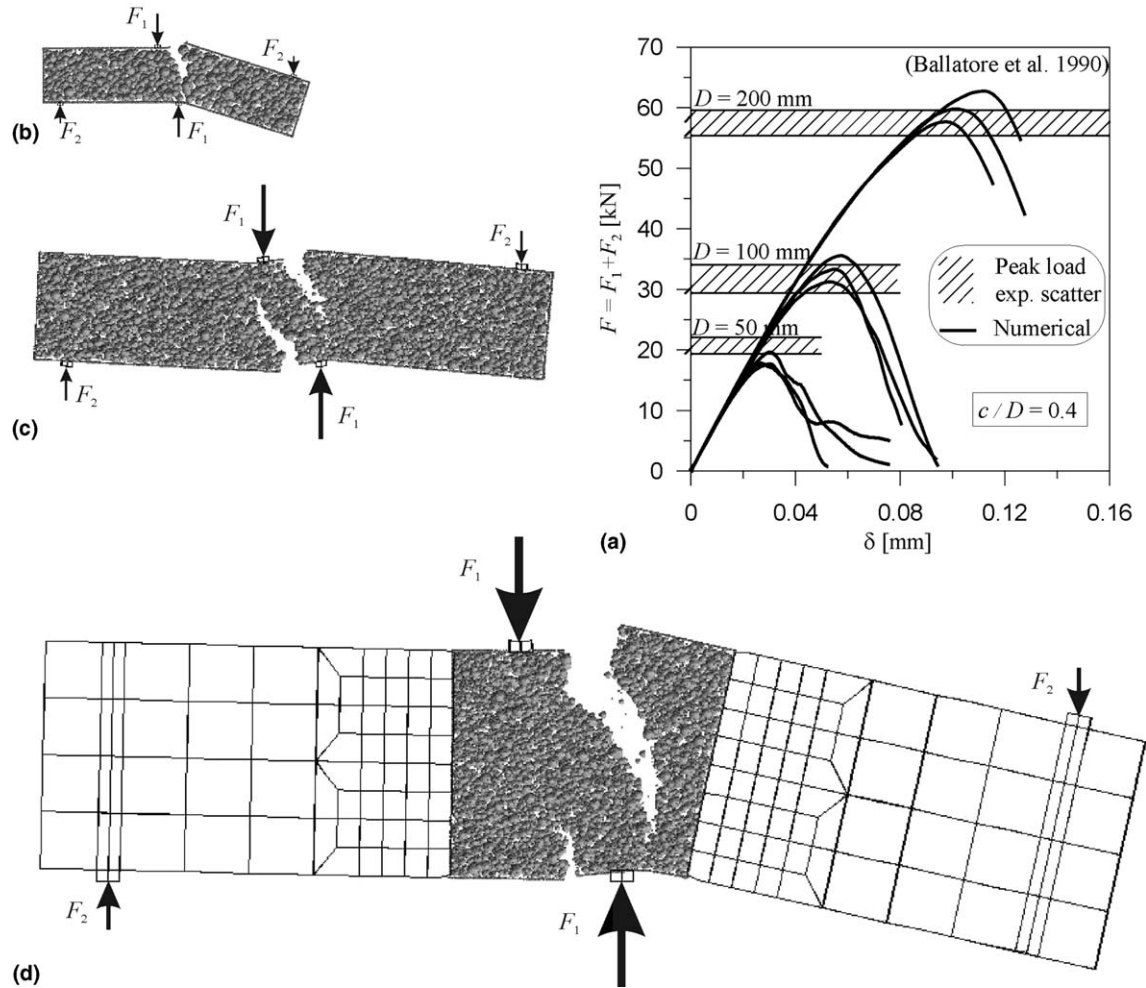
Fig. 10. Four-point shear test with $c/D = 0.4$: (a) load–displacement curves, (b)–(d) displaced configuration at failure for $D = 50$ mm, 100 mm, 200 mm, respectively.

The reduction of the internal energy while the external energy is still increasing ($F d\delta > 0$) causes an instability, which, in turn, leads to a dynamic evolution of the system. This instability is what causes the difference in the mode of failure of the large-size specimens.

Fig. 12 compares the evolution of damage for large- (Fig. 12a and b) and medium- (Fig. 12c and d) size specimens. Up to the peak, in both cases two inclined cracks are found to propagate from the notch tips. Then, for the medium-size specimen, they both propagate further towards the opposite sides of the specimen. For the large-size specimen, in which instability occurs, one crack stops and the other keeps propagating towards the specimen edge, which then leads to failure.

As far as the small-size specimen ($D = 50$ mm) is concerned, the numerical simulations predict the development of only one fracture (Fig. 10a) whereas experimentally the growth of two fractures was observed. This discrepancy may be attributed to the fact that the CSL model cannot capture accurately the effect of defects or notches not larger than the maximum aggregate size. For the smallest specimens this is exactly the case since $a = 10$ mm $< d_a$.

7. Nooru-Mohamed test

Fig. 13a depicts the setup of the mixed-mode fracture test of [22]. A double-notched prism (200 mm $\times$ 200 mm $\times$ 50 mm) with two 25 mm deep notches, was loaded simultaneously in tension (T) and shear (S). Various proportional and non-proportional loading paths were followed, with both displacement and load controls. Here we consider loading paths 4 and 6, which are frequently used as benchmarks to check the ability of constitutive models to simulate complex crack paths. Path 4 is non-proportional. The shear force, F_S, is first increased up to a certain value while tensile force F_T is kept zero. Afterwards, the shear force is kept constant while a tensile force is applied under displacement control until the specimen fails completely. In Nooru-Mohamed's experiments, the shear force was kept constant at 5 kN $\approx F_{S,max}/6$ (path-4a), 10 kN $\approx F_{S,max}/3$ (path-4b) and $F_{S,max} = 27.38$ kN (path-4c), where $F_{S,max}$ is the maximum shear force that the specimen
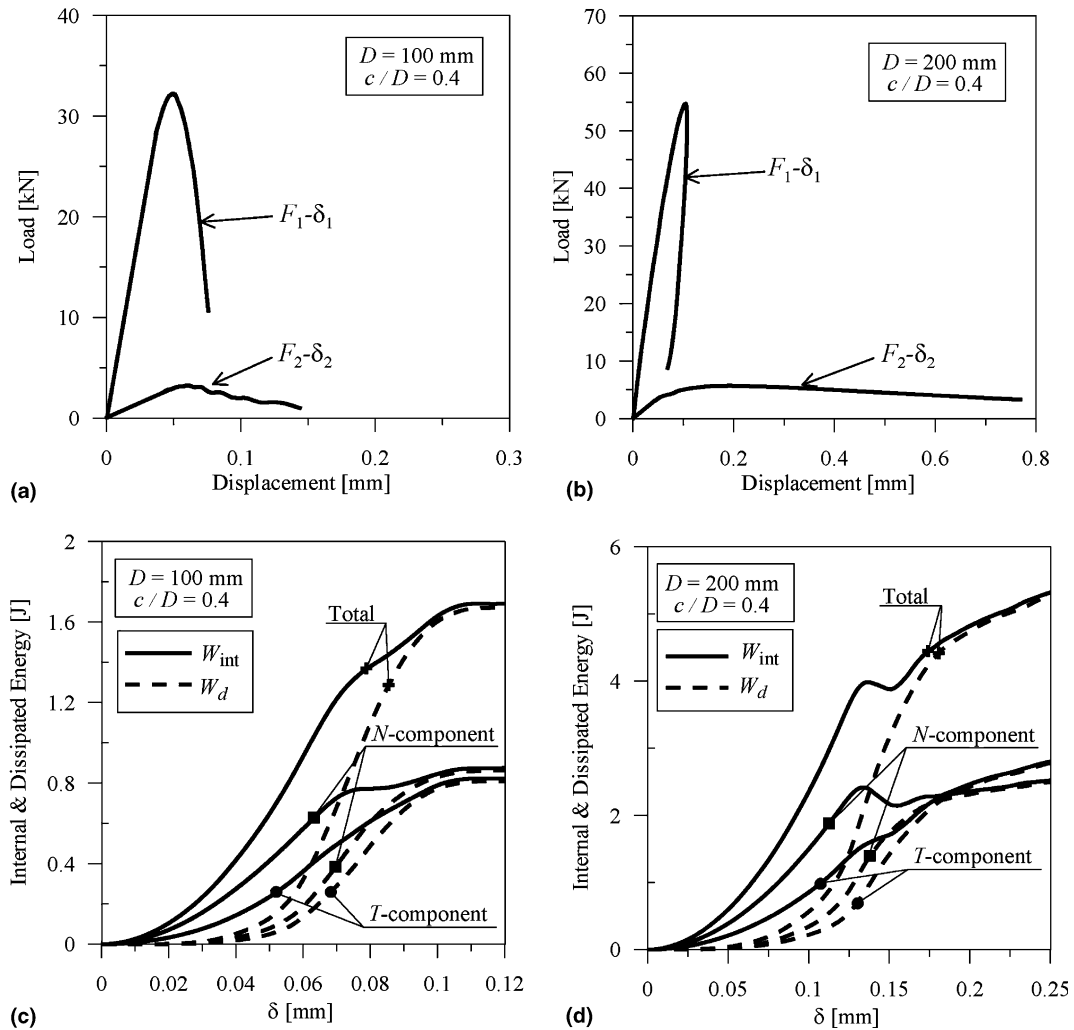
Fig. 11. (a,b) Load–displacement curves at the top supports, and (c,d) evolution of dissipated energy for $D = 100$ mm, and $D = 200$ mm, respectively.

could sustain in absence of the tensile force. Paths 6 is, by contrast, proportional, with the ratio of tensile displacement δ_T to shear displacement δ_S being constant. Nooru-Mohamed's tests featured three different values of this ratio: $\delta_T/\delta_S = 1$, $\delta_T/\delta_S = 2$, and $\delta_T/\delta_S = 3$, labeled as path 6a, 6b and 6c, respectively.

The numerical lattice simulations of these mixed-mode tests use the same model parameters as optimized in the preceding section. An *ad hoc* optimization based on the mix-design of the mortar for these experiments (with the maximum aggregate size of 2 mm) could, in theory, be done. However, the computational cost would be too high, due to the huge number of aggregates that would have to be randomly placed throughout the specimen. A quantitative, as well as qualitative, comparison between the present numerical results and the experimental data is nevertheless meaningful because the macroscopic properties of the Nooru-Mohamed mortar are quite similar to the properties of Ballatore's concrete. This similarity is also confirmed by direct comparison between the experimental and numerical responses to simple loading paths. For a pure-shear loading path, the model gives the maximum load of 32.80 kN, which is not too different from the experimental value (27.38 kN). For the pure tension path, the model gives the maximum load of 17.40 kN, which is quite close to the experimental value of 16.82 kN (see also Fig. 13b, path-0).

Fig. 13b compares the numerical and experimental responses under tension (displacement δ_T is measured over the base length of 65 mm, Fig. 13a). For loading paths 4a and 4b, the model predicts the maximum tensile force reductions (due to the presence of shear force) to be about 9% and 22%, respectively. The measured reductions were 11.9% and 29.5%, respectively.

For loading path 6c, the tensile load carrying capacity is completely lost and the tensile force becomes even negative, because of concrete dilatancy. In this regard, note that the adopted constitutive law at the meso-level does not simulate the dilatancy directly. The source of the observed macroscopic dilatancy is the aggregate interlock, which is automatically captured by the model.
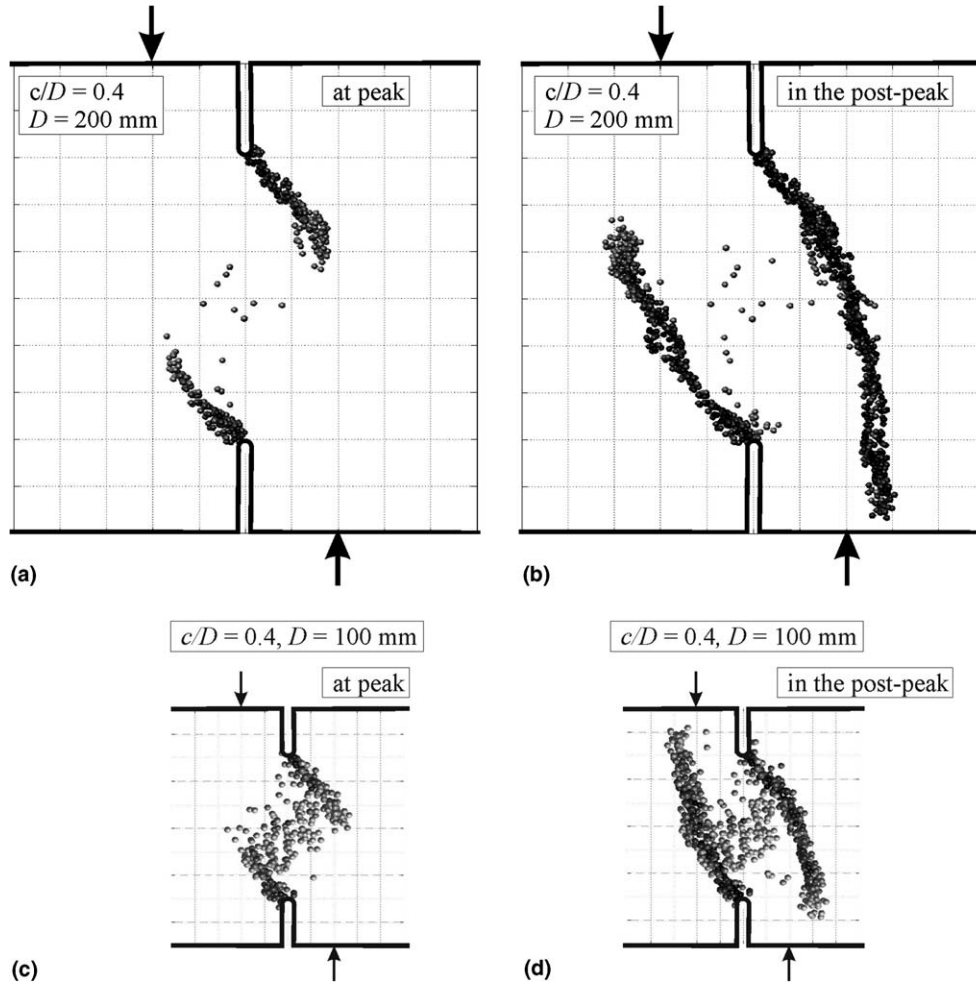
Fig. 12. Damage distribution: (a,c) at peak, and (b,d) in the post-peak for $D = 100$ mm, and $D = 200$ mm, respectively.

The effect of dilatancy is further highlighted by loading paths 6. Fig. 13c and d show the load–displacement curves obtained in shear and tension, respectively, for the loading paths 6a, 6b and 6c. The agreement between the experimental and numerical results is good for tension. Only for path 6a, the dilatancy has an appreciable effect, leading to a negative tensile (compressive) force in the post-peak behavior. As far as the shear behavior is concerned, the results of the simulations are not as good as those for tension (although still reasonable). This discrepancy may be attributed to the aforementioned differences in aggregate grading adopted for the model.

Deformed configurations at failure, with exaggerated displacements, are shown for paths 4a, 4b, 4c and 6a in Fig. 14a. In Fig. 14b, the simulated crack paths, indicated by the zones (shown in gray) in which energy is dissipated, are compared to the experimentally observed crack paths. As we see, the CSL model predicts the different crack paths for different loading paths quite well. In particular, it simulates the differences in crack curvature observed for the different loading paths.

8. Summary and conclusions

The CSL model simulates concrete meso-structure by means of a three-dimensional lattice in which the nodes are the centers of coarse aggregate pieces. The topology of the connections among the aggregates is obtained by three-dimensional Delaunay triangulation. Rigid body kinematics of the particles (aggregates + surrounding mortar) characterizes the deformation of each connecting strut. Fracture, friction and cohesion at the meso-level are simulated trough a damage-like constitutive relation. Dilatancy and aggregate interlock of crack faces is automatically captured by crack surface roughness.

In the present study, the formulation of the CSL model has been enhanced in five ways:

1. The meso-structure generation process has been generalized so as to include the explicit simulation of external concrete surfaces. To this end, extra nodal points are randomly generated throughout the specimen surfaces.
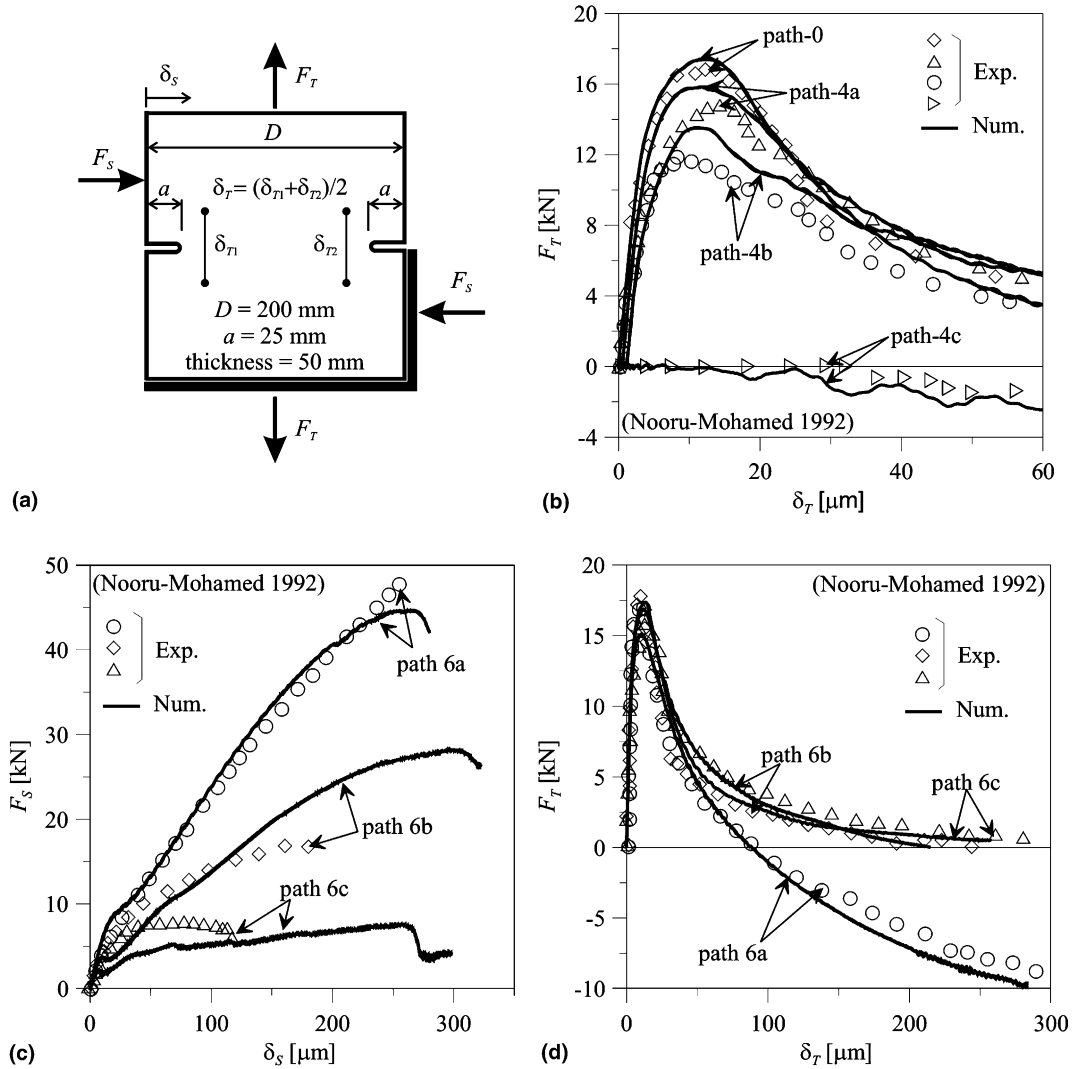
Fig. 13. Nooru-Mohamed test: (a) experimental setup, (b) response in tension for loading path-0 and loading path-4, (c) response in shear for loading path-6, (d) response in tension for loading path-6.

2. The definition of the contact area of each connecting strut has been improved by introducing a new three-dimensional domain tessellation, representing a dual complex of Delaunay triangulation. The tessellation procedure prevents the aggregates from being crossed by potential crack surfaces. This goal could not have been achieved by the well-known Voronoi tessellation.
3. The confinement effect is formulated in terms of confinement strain instead of confinement stress. This leads to a fully explicit formulation of the constitutive model.
4. A simple algorithm to apply the boundary conditions due to rigid loading platens has been developed, based on the framework of the explicit mid-point integration scheme.
5. A general procedure for coupling the lattice mesh with the usual elastic finite element mesh has been formulated. Towards this goal, two well-known numerical procedures, the master–slave approach and the static condensation, are combined.

The numerical simulations of mixed mode fracture tests, such as four point shear test and Nooru-Mohamed's test, demonstrate good prediction capability of the model, from both qualitative and quantitative viewpoints. In particular the present lattice model can

- accurately predict mixed-mode fracture propagation under complex loading paths, which produce complex crack paths;
- predict the load–displacement curves correctly;
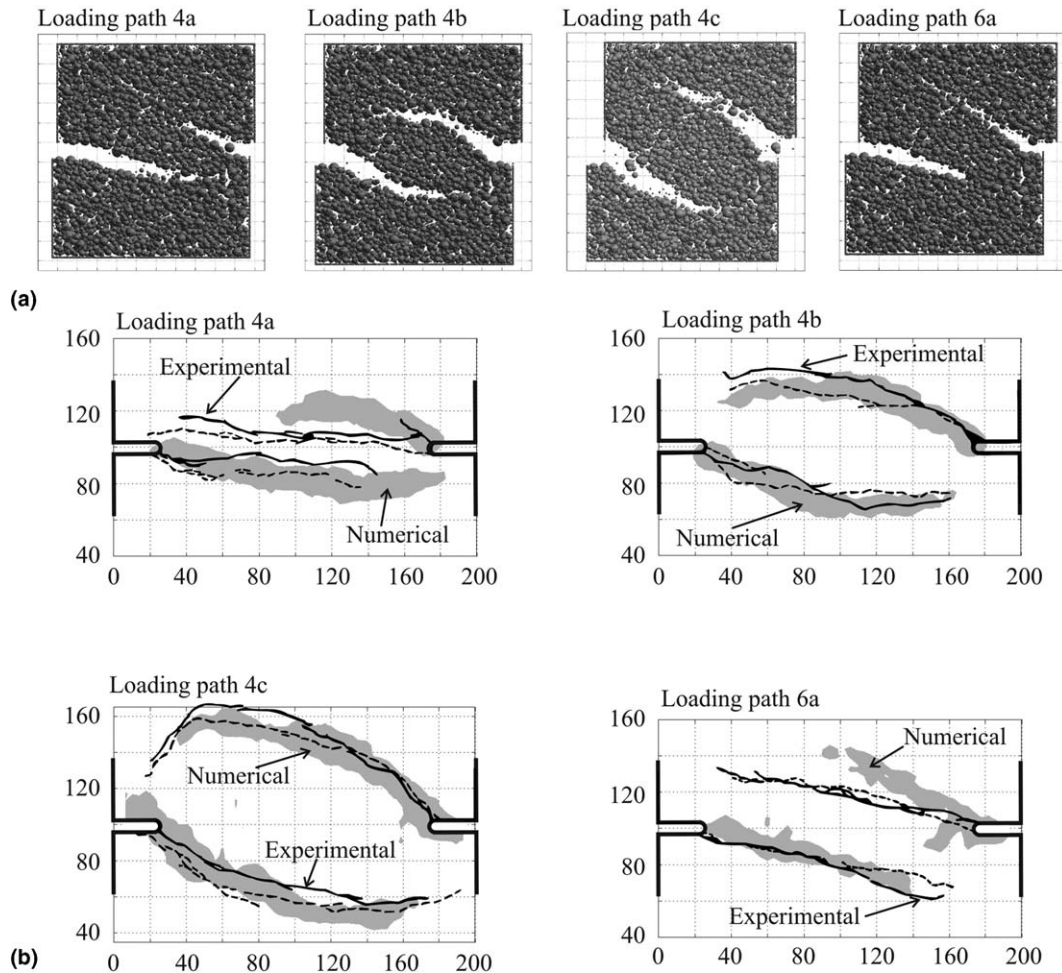- capture the loss of load carrying capacity in tension due to the presence of a pre-applied shear force;

Fig. 14. (a) Displaced configurations at failure for different loading paths. (b) Comparison between the experimental and the numerical crack path for different loading paths.

- reproduce the increase of the crack path curvature, with progressively increased pre-applied constant shear force, observed in displacement controlled tensile tests;
- capture the dilatancy effect, as well as the crack path direction, observed during proportional loading paths with displacement control.

Acknowledgements

References

[1] E. Ballatore, A. Carpinteri, G. Ferrara, G. Melchiorri, Mixed mode fracture energy of concrete, Engrg. Frac. Mech. 35 (1/2/3) (1990) 145–157.
[2] C.B. Barber, D.P. Dobkin, H.T. Huhdanpaa, The Quickhull algorithm for convex hulls, ACM Trans. Math. Softw. 22 (4) (1996) 469–483. Available from: <http://www.qhull.org>.
[3] Z.P. Bažant, B.H. Oh, Crack band theory for fracture of concrete, Matér. Construct. 16 (1983) 155–177.
[4] Z.P. Bažant, P.A. Pfeiffer, Shear fracture tests of concrete, Mater. Struct. 19 (1986) 111–121.
[5] Z.P. Bažant, P.A. Pfeiffer, Determination of fracture energy from size effect and brittleness number, ACI Mater. J. 84 (1987) 463–480.
[6] Z.P. Bažant, M.R. Tabarra, T. Kazemi, G. Pijaudier-Cabot, Random particle model for fracture of aggregate or fiber composites, J. Eng. Mech. 116 (8) (1990) 1686–1705.

[7] T. Belytschko, W.K. Liu, Nonlinear Finite Elements for Continua and Structures, John Wiley, Chichester, England, 2000.

[8] J.E. Bolander, G.S. Hong, K. Yoshitake, Structural concrete analysis using rigid-body-spring networks, J. Comput. Aided Civil Infrastruct. Engrg. 15 (2000) 120–133.

[9] J.E. Bolander, S. Saito, Fracture analysis using spring network with random geometry, Engrg. Fract. Mech. 61 (5–6) (1998) 569–591.

[10] J.E. Bolander, K. Yoshitake, J. Thomure, Stress analysis using elastically uniform rigid-body-spring networks, J. Struct. Mech. Earthquake Engrg. JSCE 633 (I-49) (1999) 25–32.

[11] G.T. Camacho, M. Ortiz, Computational modelling of impact damage in brittle materials, Int. J. Solids Struct. 33 (20–22) (1996) 2899–2938.

[12] I. Carol, C.M. López, O. Roa, Micromechanical analysis of quasi-brittle materials using fracture-based interface elements, Int. J. Numer. Method Engrg. 52 (2001) 193–215.

[13] G. Cusatis, G. Di Luzio, M. Rota, Simulation of headed anchor failure, in: N. Bićanić, R. de Borst, H. Mang, G. Meschke (Eds.), Computational Modeling of Concrete Structures (Proc., EURO-C 2003 Conference), St. Johann im Pongau, Austria, March 2003, A.A. Balkema, The Netherlands, pp. 683–688, ISBN 9058095363.

[14] G. Cusatis, M. Polli, L. Cedolin, Mesolevel analysis of fracture tests for concrete, in: V.C. Li, C.K.Y. Leung, K.J. Willam, S.L. Billington (Eds.), Fracture Mechanics of Concrete Structures, Proceedings of the Fifth International Conference on Fracture Mechanics of Concrete and Concrete Structures—FraMCoS-5, Vail Cascade Resort, Vail Colorado, Ia-FraMCos, USA, April 2004, pp. 345–351.

[15] G. Cusatis, Z.P. Bažant, L. Cedolin, Confinement-shear lattice model for concrete damage in tension and compression: I, Theory J. Engrg. Mech. ASCE 129 (12) (2003) 1439–1448.

[16] G. Cusatis, Z.P. Bažant, L. Cedolin, Confinement-shear lattice model for concrete damage in tension and compression: II. Computation and validation, J. Engrg. Mech. ASCE 129 (12) (2003) 1449–1458.

[17] B. Delaunay, Sur la sphère vide, Bull. Acad. Sci. USSR(VII), Classe Sci. Mat. Nat. (1934) 793–800.

[18] Z. Hashin, P.J.M. Monteiro, An inverse method to determine the elastic properties of the interphase between the aggregate and the cement paste, Cement and Concrete Res. 32 (2002) 1291–1300.

[19] M. Jirásek, Z.P. Bažant, Macroscopic fracture characteristics of random particle systems, Int. J. Fract. 69 (3) (1995) 201–228.

[20] M. Jirásek, Z.P. Bažant, Particle model for quasibrittle fracture and application to sea ice, J. Engrg. Mech. ASCE 121 (9) (1995) 1016–1025.

[21] G. Lilliu, J.G.M. van Mier, 3D lattice type fracture model for concrete, Engrg. Fract. Mech. 70 (2003) 927–941.

[22] M.B. Nooru-Mohamed, Mixed-mode fracture of concrete: an experimental approach, Ph.D. thesis, Delft University of Technology, Delft, 1992.

[23] RILEM TC QFS (chaired by Z.P. Bažant), Quasibrittle fracture scaling and size effect—Final report, Mater. Struct. (Paris) 37 (272) (2004) 547–586.

[24] P.E. Roelfstra, H. Sadouki, F.H. Wittmann, Le béton numérique, Mater. Struct. 18 (1985) 327–335.

[25] E. Schlangen, Experimental and numerical analysis of fracture processes in concrete, Ph.D. thesis, Delft University of Technology, Delft, The Netherlands, 1993.

[26] E. Schlangen, Computational aspects of fracture simulations with lattice models, in: F.H. Wittmann (Ed.), Fracture Mechanics of Concrete Structures (Proc., FraMCoS-2 held in Zürich), Aedificatio Publ., Freiburg, Germany, 1995, pp. 913–928.

[27] E. Schlangen, J.G.M. van Mier, Shear fracture in cementitious composites, Part II: Numerical simulations, in: Z.P. Bažant (Ed.), Fracture Mechanics of Concrete Structures (Proc., FraMCoS-1), Elsevier, London, 1992, pp. 671–676.

[28] J.M. Ting, L.R. Meachum, J.D. Rowell, Effect of particle shape on the strength and deformation mechanics of ellipse-shaped granular assemblage, Engrg. Comput. 12 (1995) 99–108.

[29] P. Underwood, Dynamic relaxation, in: T.J.R. Hughes, T.B. Belytschko (Eds.), Computational Methods for Transient Analysis, vol. 5, Elsevier Science Publishers B.V., Netherlands, 1983, pp. 245–265.

[30] J.G.M. van Mier, A. Vervuurt, E. Schlangen, Boundary and size effects in uniaxial tensile tests: a numerical and experimental study, in: Z.P. Bažant, Z. Bittnar, M. Jirásek, J. Mazars (Eds.), Fracture and Damage in Quasibrittle Structures (Proc., NSF Workshop, Prague), E&FN Spon, London, 1994, pp. 289–302.

[31] F.H. Wittmann, P.E. Roelfstra, C.L. Kamp, Drying of concrete: an application of the 3L-approach, Nucl. Engrg. Des. 105 (1988) 185–198.

[32] A. Zubelewicz, Z.P. Bažant, Interface modeling of fracture in aggregate composites, ASCE J. Engrg. Mech. 113 (11) (1987) 1619–1630.